

## Li self-diffusion and ion conductivity in congruent $\text{LiNbO}_3$ and $\text{LiTaO}_3$ single crystals

Claudia Kofahl,<sup>1</sup> Lars Dörrer,<sup>1</sup> Brendan Muscutt,<sup>2</sup> Simone Sanna,<sup>2,3</sup> Stepan Hurskyy,<sup>4</sup> Uliana Yakhnevych,<sup>4</sup> Yuriy Suhak,<sup>4</sup> Holger Fritze,<sup>4</sup> Steffen Ganschow,<sup>5</sup> and Harald Schmidt<sup>1,6,\*</sup>

<sup>1</sup>*Institut für Metallurgie, AG Festkörperkinetik, Technische Universität Clausthal, Robert-Koch-Straße 42, 38678 Clausthal-Zellerfeld, Germany*

<sup>2</sup>*Institut für Theoretische Physik, Justus-Liebig-Universität Gießen, Heinrich-Buff-Ring 16, 35392 Gießen, Germany*

<sup>3</sup>*Center for Materials Research (ZfM/LaMa), Justus-Liebig-Universität Gießen, Heinrich-Buff-Ring 16, 35392 Gießen, Germany*

<sup>4</sup>*Institut für Energieforschung und Physikalische Technologien, Technische Universität Clausthal, Am Stollen 19, 38640 Goslar, Germany*

<sup>5</sup>*Leibniz-Institut für Kristallzüchtung, Max-Born-Str. 2, 12489 Berlin, Germany*

<sup>6</sup>*Clausthaler Zentrum für Materialtechnik (CZM), Technische Universität Clausthal, Leibnizstraße 9, 38678 Clausthal-Zellerfeld, Germany*



(Received 3 November 2022; accepted 28 February 2023; published 23 March 2023)

Lithium niobate and lithium tantalate crystals are technologically important metal oxides with exceptional combinations of ferroelectric, piezoelectric, acoustic, optical, and electrical properties. The self-diffusion of both, the ionic constituents and the underlying point defects, is especially important for the overall electrical conductivity. To get insight into their dynamics, we investigate in this work Li self-diffusion in congruent  $\text{LiNbO}_3$  and  $\text{LiTaO}_3$  single crystals from different suppliers up to a temperature of 800 °C, using isotope-enriched  $^6\text{LiNbO}_3$  and  $^6\text{LiTaO}_3$  tracer layers in combination with secondary ion mass spectrometry depth-profile analysis. The diffusivities of the two isostructural materials are identical within error limits and can be described by the Arrhenius law with an activation energy of 1.35 eV in the range from 150° to 800 °C. Furthermore, the electrical conductivity is determined between 400 °C and 600 °C and can be described by an activation energy of about 1.34 eV. This is in excellent agreement with the energy barrier for the diffusion of a single Li vacancy as determined by nudged elastic band calculations based on density-functional theory. The Li-ion conductivities calculated from the diffusivities in  $\text{LiNbO}_3$  and  $\text{LiTaO}_3$  are identical within the error margins with the overall conductivities obtained from impedance spectroscopy measurements. This indicates that the migration of  $\text{Li}^+$  is able to explain the overall electrical conductivity below 600 °C down to 180 °C.

DOI: [10.1103/PhysRevMaterials.7.033403](https://doi.org/10.1103/PhysRevMaterials.7.033403)

### I. INTRODUCTION

Lithium niobate ( $\text{LiNbO}_3$ ) and its isostructural counterpart lithium tantalate ( $\text{LiTaO}_3$ ) are technologically important synthetic oxides, with an extraordinary combination of ferroelectric, piezoelectric, acoustic, optical, as well as ion, conductivity properties [1–4]. The large ferroelectric, pyroelectric, and piezoelectric coefficients are due to a vertical displacement of the cations from the center of the oxygen octahedra in the hexagonal crystal structure (space group  $R3c$ ) [5–8]. Both materials can be grown with variable Li content, ranging within a wide solid solution region from 44 mol. % to about 50.5 mol. %  $\text{Li}_2\text{O}$  [9,2]. Single crystals produced by the Czochralski method commonly show the congruent composition of about 48.6 mol. %  $\text{Li}_2\text{O}$ . The change of composition from the lithium poor to the stoichiometric composition results in significant changes in the physical properties of the system [10], including the Curie temperature, the ferroelectric coercive field, photorefractive properties, and, most important for the subsequent discussion, defect concentrations. The formation of different, charge-neutral defect clusters has been proposed to model the congruent composition [5, 11–14]. While the commonly accepted model for the realization of the congruent composition in  $\text{LiNbO}_3$  consists of

a niobium antisite, which is compensated by four lithium vacancies ( $\text{Nb}_{\text{Li}}^{\bullet\bullet} + 4\text{V}_{\text{Li}}^{\bullet}$ ) [12,15,14], a more complex defect structure is suggested for  $\text{LiTaO}_3$  [16].

For many applications of lithium niobate, self-diffusion of the constituents is of high importance. In particular, diffusivities are a measure for ionic transport properties and consequently for the ion conductivity. At low and medium temperatures up to 500 °C, Li is expected to be the most mobile species. Here, we investigate Li self-diffusion in  $\text{Li}_2\text{O}$ -deficient (congruent)  $\text{LiNbO}_3$  and  $\text{LiTaO}_3$  single crystals from different suppliers for temperatures up to 800 °C using secondary ion mass spectrometry. The results are compared to conductivity measurements performed by impedance spectroscopy and theoretical calculations.

### II. METHODOLOGY

#### A. Experiment details

The congruent  $\text{LiNbO}_3$  and  $\text{LiTaO}_3$  single crystals under investigation were supplied by Precision Micro-Optics Inc (USA) and by CrysTec GmbH (Berlin, Germany). Polished Z-cut wafers were cut into  $6 \times 5 \times 0.5\text{-mm}^3$  pieces. In addition, X-cut plano-plano  $\text{LiTaO}_3$  disks of 0.5-mm thickness and 16-mm diameter were supplied by the Leibniz-Institut für Kristallzüchtung (Berlin, Germany).

Tracer deposition was carried out by depositing a 0.1–1- $\mu\text{m}$  thin layer of isotope-enriched  $^6\text{LiNbO}_3$  or  $^6\text{LiTaO}_3$

\*Corresponding author: [harald.schmidt@tu-clausthal.de](mailto:harald.schmidt@tu-clausthal.de)

on the single crystal by ion-beam sputtering, using a commercial setup (IBS 681, Gatan) equipped with two Penning ion sources. Deposition was done at 5 kV and a current of about 180  $\mu\text{A}$  in argon at an operating pressure of  $5 \times 10^{-3}$  mbar. The base vacuum was better than  $5 \times 10^{-7}$  mbar.

The sputter targets were prepared by solid-state syntheses as described in Ref. [17]. Due to the fact that the tracer layer and single crystal have approximately the same chemical composition, pure isotope interdiffusion is expected to be measured during the diffusion experiments. For the latter, the coated samples were annealed in synthetic air in a rapid thermal annealing furnace, which allows fast heating and cooling rates and consequently short isothermal annealing times down to 1 min. Annealing was done at temperatures between 250 °C and 800 °C. The samples were preannealed in synthetic air prior to tracer deposition at the same temperature at which the diffusion experiments were performed for a time period significantly higher than the diffusion time.

The inward diffusion of the  ${}^6\text{Li}$  from the sputtered layer into the single crystal was monitored by secondary ion mass spectrometry (SIMS) using a Cameca ims-3f machine. An  $\text{O}^-$  primary ion beam (15 keV, 40–180 nA) was used in order to prevent electrical charging during the measurement. The sputtered area was about  $250 \mu\text{m} \times 250 \mu\text{m}$ . For further processing in a double-focused mass spectrometer, the signal resulting from an area of about  $60 \mu\text{m} \times 60 \mu\text{m}$  in the center was used in order to exclude effects resulting from the crater edge.

In the depth-profiling mode, the secondary ion intensities of  ${}^6\text{Li}^+$  and  ${}^7\text{Li}^+$  ions were recorded as a function of sputter time. Since the two Li isotopes are chemically identical (neglecting the small isotope effect), for diffusion analysis the intensity of the signals is converted into  ${}^6\text{Li}$  atomic fractions  $c(x, t)$  according to

$$c(x, t) = \frac{I({}^6\text{Li})}{I({}^6\text{Li}) + I({}^7\text{Li})}. \quad (1)$$

Depth calibration was performed by measuring the crater depth with a mechanical profilometer (Tencor, Alphastep).

The electrical impedance was determined using Z-cut samples from the Precision Micro-Optics wafer mentioned above. Moreover, impedance spectra of X-cut samples of the same crystal provider are presented. Square-shaped electrodes with an area  $A = 5 \times 5 \text{ mm}^2$  and a thickness of about  $3 \mu\text{m}$  were deposited by screen printing (print ink C-3620, Heraeus GmbH & Co. KG, Hanau, Germany) on both sides of the plates and annealed at a temperature of 850 °C for 1 h. Concerning the samples from the Institut für Kristallzüchtung, Pt electrodes with a thickness of  $\sim 3 \mu\text{m}$  are deposited by screen printing (print ink: Ferro Corporation, No. 6412 0410). After screen printing, the specimens are annealed at 1000 °C for about 30 min.

The actual impedance measurements were done in air while lowering the temperature with 1 K/min from about 600 °C to 200 °C. The impedance of the samples was determined by AC impedance spectroscopy in the frequency range from 1 Hz to 1 MHz using an impedance/gain-phase analyzer (Solartron 1260). An electrical equivalent-circuit model consisting of a constant-phase element (CPE) connected in

parallel with a bulk resistance  $R_B$  was fitted to the measured data. Subsequently, the bulk conductivity  $\sigma$  was calculated from the relation

$$\sigma = t/(A \times R_B), \quad (2)$$

with the sample thickness  $t = 0.5 \text{ mm}$  and the electrode area  $A$  given above. The lead resistance, arising from cables/mounting, was very low and, therefore, neglected in the fitting procedure. More information about the measurement and data evaluation approach can be found in Refs. [18,19].

## B. Computational details

The Vienna *Ab initio* Simulation Package [20,21] was employed to evaluate the structural and electronic properties of isolated Li vacancies in  $\text{LiNbO}_3$  and  $\text{LiTaO}_3$  within density-functional theory. Isolated, negatively charged vacancies were simulated within  $3 \times 3 \times 3$  repetitions of the primitive unit cell (i.e., 270 atoms), which models a vacancy concentration of 1.85 mol. %. Projected augmented-wave potentials [22,23] which explicitly consider the  $2s^1$  electron for Li, the  $2s^2 2p^4$  electrons for O, and the  $4p^6 4d^4 5s^1$  and  $5p^6 5d^3 6s^2$  electrons for Nb and Ta, respectively, were used to describe the ion-electron interaction. The generalized gradient approximation [24] in the Perdew-Burke-Ernzerhof formulation [25,26] was used to describe the electronic many-body interactions. Plane waves up to a cutoff of 440 eV were used as basis for the expansion of electron wave functions. To perform the energy integration in the Brillouin zone,  $2 \times 2 \times 2$   $k$ -point meshes generated with the Monkhorst-Pack algorithm [27] and centered at the  $\Gamma$  point were employed. The atomic positions were relaxed until the self-consistently calculated residual Hellmann-Feynman forces [28] are lower than 0.01 eV/Å. Convergence tests show that this approach leads to converged results concerning total energies and forces. Minimum-energy paths and energy barriers for the vacancy diffusion were calculated by the nudged elastic band (NEB) method [28–32]. We make use of eight images that are initially equidistantly distributed along the considered diffusion path. All considered pathways for the Li vacancy diffusion are described in Sec. III.

## III. RESULTS

First, the results of the diffusion experiments are discussed. The  ${}^6\text{Li}$  atomic fraction as a function of sputter depth as measured by SIMS is exemplarily illustrated in Fig. 1 for an as-deposited sample and samples diffusion annealed for (a)  $\text{LiNbO}_3$  at 800 °C and (b)  $\text{LiTaO}_3$  at 700 °C. During annealing the  ${}^6\text{Li}$  tracer penetrates into the single crystal typically to depths in the micrometer range.

Experimentally determined depth profiles after annealing can be described by the following solution of Fick's second law for self-diffusion across an interface [33]:

$$c(x, t) = c_\infty + \frac{(c_0 - c_\infty)}{2} \left[ \text{erf}\left(\frac{h+x}{R}\right) + \text{erf}\left(\frac{h-x}{R}\right) \right], \quad (3)$$

where  $c_\infty \approx 0.08$  is the natural abundance of  ${}^6\text{Li}$  in the single crystal and  $c_0 = 0.95$  that in the tracer layer. The original thickness of the as-deposited tracer layer is denoted as  $h$  and

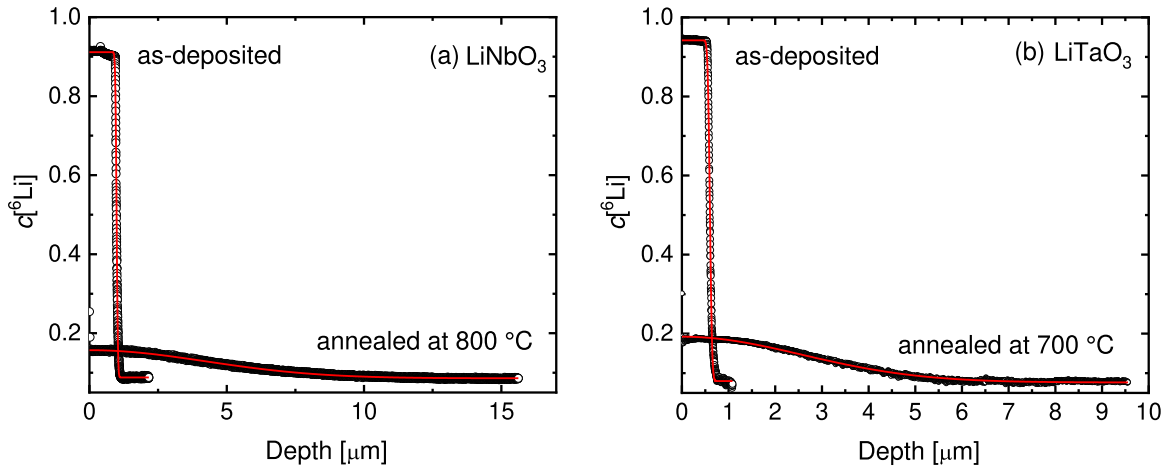


FIG. 1. Atomic fraction of  ${}^6\text{Li}$  as a function of depth after deposition and annealing for (a)  $\text{LiNbO}_3$  at  $800^\circ\text{C}$  for 108 s and (b)  $\text{LiTaO}_3$  at  $700^\circ\text{C}$  for 127 s. A least-squares fit of Eq. (3) to the experiment data is also indicated in red.

is between  $0.1\text{--}1\ \mu\text{m}$ , depending on the sample under investigation. The quantity  $R$ , characteristic for the depth of the tracer profile, is treated as a fit parameter. The self-diffusivity  $D$  at time  $t$  is determined from the difference in  $R$  of the diffusion profile and of the starting profile according to  $D = [R^2(t) - R^2(0)]/4t$  [33]. The diffusivities determined using this method are plotted as a function of reciprocal temperature in Fig. 2 for both materials and two suppliers (CrysTec and Precision Micro-Optics). The recorded data are in excellent agreement with measurements of our group on samples from CrysTec available in the literature below  $500^\circ\text{C}$ , which are also included in Fig. 2 [17,34]. A comparison of the results obtained on crystals of the two different suppliers (Precision

Micro-Optic and CrysTec) at  $250^\circ\text{C}$  and  $600^\circ\text{C}$  reveals that the diffusivities are identical within error limits. The error limits attributed to each diffusivity result in sum from the uncertainty in crater-depth determination, from fitting, and from measuring at different locations on the sample surface with locally slightly differing diffusion behavior. At a temperature of  $600^\circ\text{C}$  we further compared crystals which were preannealed as described in Sec. II A to those which were not preannealed, which were preannealed in argon or which were preannealed in pure oxygen. No differences were found at this temperature.

The diffusivities of each type of material follow the Arrhenius law:

$$D = D_0 \exp(-\Delta E/kT), \quad (4)$$

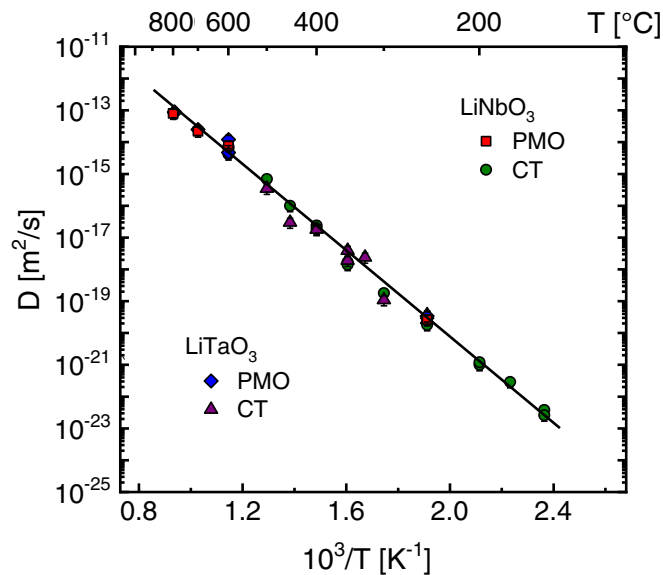


FIG. 2. Tracer diffusivities of Li in congruent  $\text{LiNbO}_3$  and  $\text{LiTaO}_3$  single crystals as a function of reciprocal temperature as measured by our group. Shown are diffusivities measured on congruent crystals of two different manufacturers, namely CrysTec (CT) and Precision Micro-Optics (PMO). The straight line corresponds to a fit of all data to Eq. (4).

in the broad temperature range between  $150^\circ\text{C}$  and  $800^\circ\text{C}$  over several orders of magnitude. An activation energy ( $\approx$  activation enthalpy) of  $\Delta E = (1.35 \pm 0.02)$  eV and a preexponential factor of  $D_0 = 3.1 \times 10^{-7}$   $\text{m}^2/\text{s}$  (error:  $\ln D_0/\text{m}^2/\text{s} = \pm 0.34$ ) is derived for  $\text{LiNbO}_3$ . Both quantities are identical to those found for literature data on diffusivities below  $500^\circ\text{C}$  [17]. This demonstrates that no change of the diffusion mechanism occurs up to  $800^\circ\text{C}$ . Note that using the method of neutron reflectometry additional diffusivities were determined in the temperature range between  $106^\circ\text{C}$  and  $250^\circ\text{C}$  [35] in agreement with the present results. Including these data into the fit with Eq. (3), the same activation energy is obtained within error limits.

Similarly to  $\text{LiNbO}_3$ , the results on congruent  $\text{LiTaO}_3$  crystals, provided by two different manufacturers, are also shown in Fig. 2, which are again identical to each other and to those of  $\text{LiNbO}_3$  within error limits. Fitting the diffusivities solely for  $\text{LiTaO}_3$ , an activation energy of  $\Delta E = (1.33 \pm 0.04)$  eV and a preexponential factor of  $D_0 = 1.7 \times 10^{-7}$   $\text{m}^2/\text{s}$  (error:  $\ln D_0/\text{m}^2/\text{s} = \pm 0.66$ ) is derived. Note that for  $\text{LiTaO}_3$  (in contrast to  $\text{LiNbO}_3$ ) the Curie temperature is at about  $600^\circ\text{C}\text{--}660^\circ\text{C}$  [36,37], within the range of our diffusivity measurements. However, we do not see any anomaly in Li diffusivities close to the transition between the paraelectric and ferroelectric phase. Nevertheless, for a clear statement a

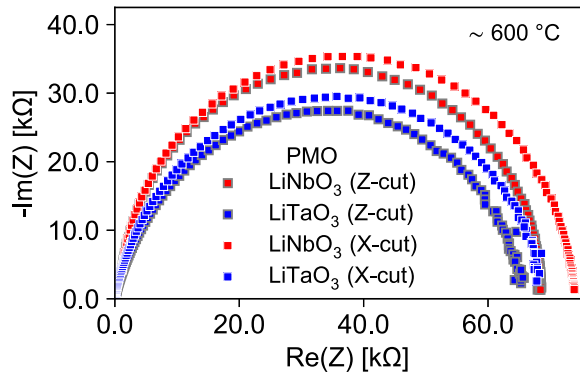


FIG. 3. Examples for impedance spectra of differently oriented LiNbO<sub>3</sub> and LiTaO<sub>3</sub> samples from PMO in the frequency range from 10 Hz to 1 MHz (Z cut: 600 °C; X cut: 603 °C).

higher number of data points is necessary, which will be the subject of subsequent studies.

The electrical conductivity is extracted from impedance spectra as shown exemplarily in Fig. 3 for X-cut and Z-cut samples. Thereby, the low-frequency intercept of the fitted  $R_B$ -CPE semicircles in the complex impedance plane are interpreted as bulk resistance  $R_B$  and subsequently converted into the bulk conductivity  $\sigma$  using Eq. (2). Below 10 Hz, the impedance data scatter, so that the evaluation was carried out above this frequency only. Further, below about 400 °C the impedance exceeds the measurement range of the device and therefore could not be determined. The semicircles show slight depression which corresponds to exponents of the CPEs of 0.99 and 0.95 for LiNbO<sub>3</sub> and LiTaO<sub>3</sub>, respectively. It results from slightly nonideal capacitances and is, however, not relevant for further discussion as the low-frequency intercept of the semicircle is virtually not influenced.

The temperature-dependent electrical conductivity is shown in Fig. 4 in form of the conductivity-temperature product. The latter results for dominating ionic transport as we (see

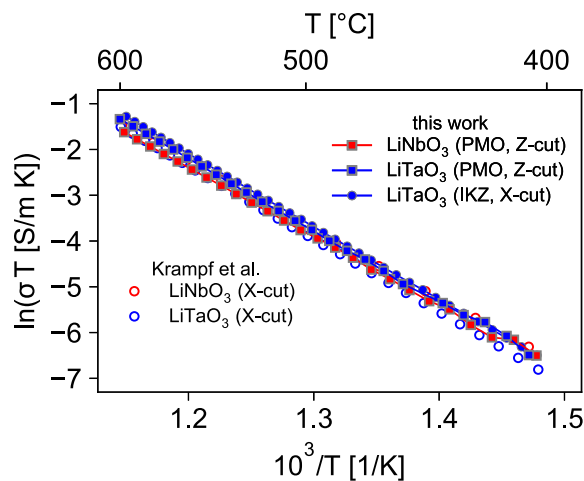


FIG. 4. Conductivity-temperature product for LiNbO<sub>3</sub> and LiTaO<sub>3</sub> in the temperature range from 400 °C to 600 °C. IKZ refers to the Leibniz-Institut für Kristallzüchtung. Further, the literature data of Krampf *et al.* [37] are given.

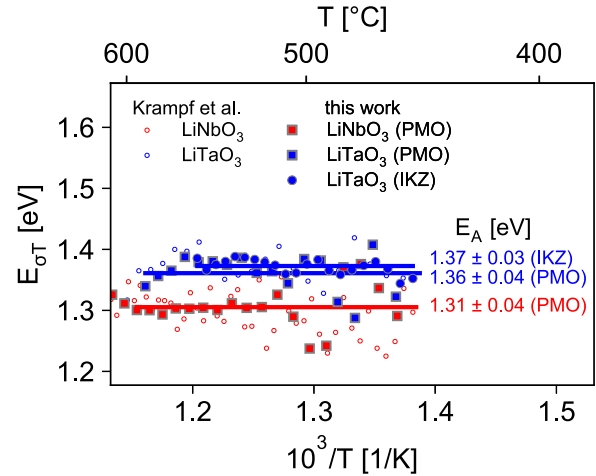


FIG. 5. Slopes  $E_{\sigma T}$  (solid symbols) and activation energies  $E_A$  (lines) for LiNbO<sub>3</sub> and LiTaO<sub>3</sub> samples from PMO and IKZ in comparison to slopes from Krampf *et al.* [37] (open symbols).

below) and others found [38–40] for LiNbO<sub>3</sub> and LiTaO<sub>3</sub> in a straight line in the Arrhenius representation. In case of LiTaO<sub>3</sub> the measurements done below 600 °C reflect the behavior of the ferroelectric phase. Data acquisition during cooling of the samples revealed a constant slope of  $\sigma T$  in the Arrhenius diagram and, therefore, no evidence of delayed transition from the paraelectric to the ferroelectric phase.

First, it is obvious that the conductivities of LiNbO<sub>3</sub> and LiTaO<sub>3</sub> are also quite similar. Slight differences in the slope are visible only, which can be explained by the measurement uncertainty of up to 5%. Consequently, based on the present uncertainty analysis there are no significant differences. Furthermore, there is virtually no difference between the respective crystals of different manufacturers. Finally, within the uncertainty of the measurement, anisotropy of electrical conductivity as observed by Ref. [41] is not found, but could not be excluded.

As the curves of the conductivity-temperature product appear to be linear in the Arrhenius representation according to

$$\sigma T = \sigma_0 \exp[-E_A/(kT)], \quad (5)$$

a single activation energy  $E_A$  is suspected. Here,  $\sigma_0$ ,  $k$ , and  $T$  represent the preexponential constant, the Boltzmann constant, and the absolute temperature, respectively. In order to prove this suspicion, the slope

$$E_{\sigma T} = -k \frac{\partial \ln(\sigma T)}{\partial \ln(1/T)} \quad (6)$$

is calculated in the temperature range from 400 °C to 600 °C. Below about 450 °C the data points scatter, so that the increase in Fig. 5 is shown above this temperature only. Here, the slope is nearly constant. Consequently, the activation energy can be calculated by averaging the slopes. For LiNbO<sub>3</sub> and LiTaO<sub>3</sub> values of  $(1.31 \pm 0.04)$  and  $(1.36 \pm 0.04)$  eV follow, respectively. Considering the measurement uncertainty, the values agree with those of lithium diffusion very well ( $\Delta E \approx E_A$ ).

For a comparison of the measured electrical conductivities and the Li diffusivities, we used the diffusivities shown in Fig. 2 to calculate corresponding ion conductivities of Li using the Nernst-Einstein relation,

$$\sigma_{Li} = \frac{Dnq^2}{kT}, \quad (7)$$

where  $n$  denotes the number density of the conducting  $Li^+$  species ( $1.89 \times 10^{22} \text{ cm}^{-3}$  for  $LiNbO_3$  and  $1.86 \times 10^{22} \text{ cm}^{-3}$  for  $LiTaO_3$ ),  $q = e$  the electrical charge,  $k$  the Boltzmann constant, and  $T$  the temperature. Since oxygen [42] and niobium [43] diffusivities in  $LiNbO_3$  are more than five orders of magnitude lower than that of Li (below  $800^\circ\text{C}$ ),  $Li^+$  is assumed to be the only ionic charge carrier in that temperature range. The results are plotted in Fig. 6 for comparison. For  $LiNbO_3$  [Fig. 6(a)] it can be seen that the conductivities calculated from the Li diffusivities are identical within error limits to the conductivities measured by impedance spectroscopy between  $180^\circ\text{C}$  and  $600^\circ\text{C}$  for different suppliers. This result indicates that the migration of  $Li^+$  is able to explain the overall electrical conductivity below  $600^\circ\text{C}$ . The error limits attributed to the diffusivities still allow other species to contribute at least partially to conductivities in the several percent range. This is particularly important for impurity hydrogen ions: Although they occupy different lattice sites than Li [44,45], they are characterized by preexponential factors [46] and diffusion pathways [47] that are comparable to those presented in this work for Li. Thus, H impurities may substantially contribute to the diffusivity, confirming that the thermal pretreatment is crucial to maintain their contribution low. The same is true for  $LiTaO_3$  as illustrated in Fig. 6(b).

In order to understand the Li diffusion in congruent  $LiNbO_3$  and  $LiTaO_3$  single crystals, two energies have to be considered, which might contribute to the activation energy of diffusion,  $\Delta E$ , at high and medium temperatures. These are the energy of Li migration via a certain defect (e.g., vacancy),  $\Delta E_m$ , and the energy of formation of this defect,  $\Delta E_f$ . Since the experimental data can be fitted with a unique Arrhenius straight line, only a single mechanism is dominant over the whole temperature range investigated. Due to the  $Li_2O$  deficient composition of the congruent single crystal, intrinsic defect structures have to be present in order to realize off stoichiometry. The currently accepted model, which explains the congruent composition of  $LiNbO_3$ , consists of a niobium antisite ion charge compensated by four lithium vacancies:  $(Nb_{Li}^{\bullet\bullet} + 4V_{Li}')$ . This model is supported by experimental x-ray- and neutron-diffraction studies [49], density-functional theory calculations [12,50], and also by diffusion experiments [51]. The result that the Li diffusivities of  $LiNbO_3$  and  $LiTaO_3$  are identical between  $250^\circ\text{C}$  and  $800^\circ\text{C}$  within error limits as well as the activation energies suggest that the defect structure  $(Nb_{Li}^{\bullet\bullet} + 4V_{Li}')$  and mole fraction of vacancies (about 4 mole %) [52] due to off stoichiometry of congruent crystals are expected to be very similar. However, it is also clear that this is no direct proof because the defect structures and vacancy concentrations were not directly measured. A differing defect structure for  $LiTaO_3$  as suggested in Ref. [16] involving Ta interstitials and Li vacancies  $(Ta_{Ta}^{\bullet} + 5V_{Li}')$  cannot be excluded, because the Li vacancy concentration would be higher by a factor of 5/4 only, which is still within error limits.

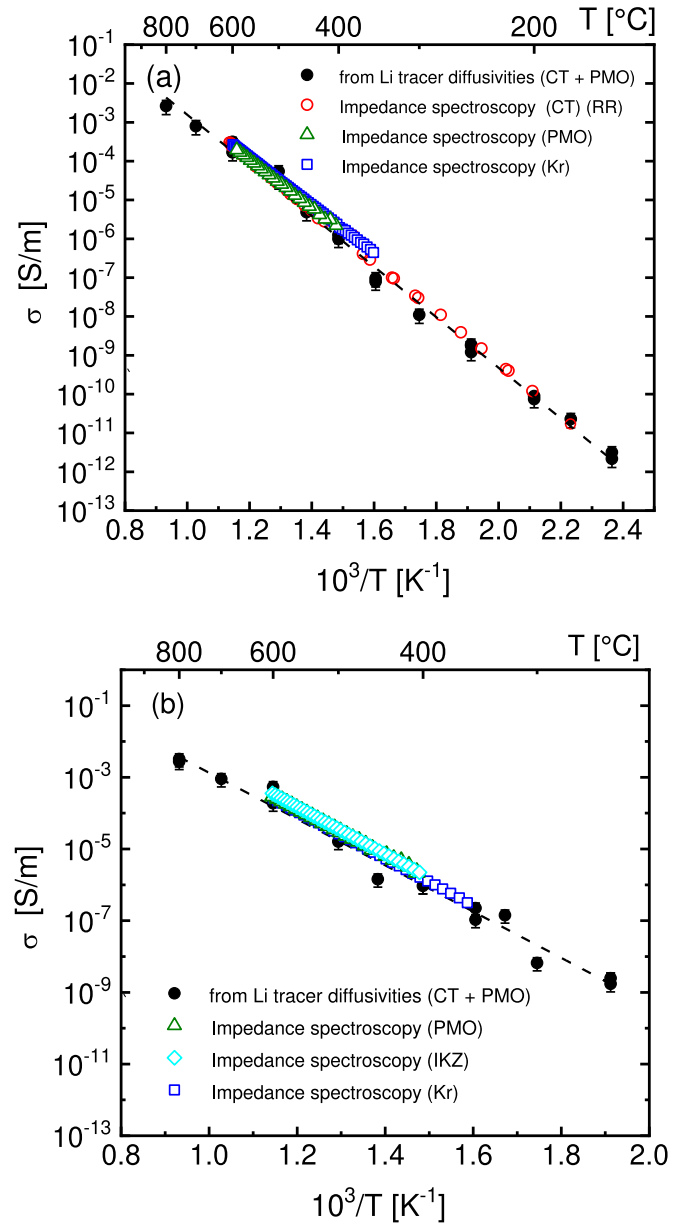


FIG. 6. Electrical conductivities as calculated from Li tracer diffusivities according to Eq. (7) together with conductivities measured by impedance spectroscopy as a function of reciprocal temperature for crystals from different manufacturers for (a)  $LiNbO_3$  and (b)  $LiTaO_3$ . CT refers to the manufacturer CrysTec. Further, RR refers to the publications Rahn *et al.* and Ruprecht *et al.* [17,48] and Kr to Krampf *et al.* [37]. Dashed lines are a guide to the eye.

For further insight, the diffusion of Li vacancies in  $LiNbO_3$  and  $LiTaO_3$  is investigated by atomistic first-principles calculations. As previous investigations have shown that the by far dominant valence state of the Li vacancies is  $-1$  [53–55,50] we only consider negatively charged vacancies.

Figure 7 schematically shows a Li vacancy and its nearest-neighbor lattice sites in a  $LiNbO_3$  crystal (the situation in  $LiTaO_3$  is analogous). Six equivalent first-nearest neighbor lattice sites are present (blue balls), at a distance of  $3.77 \text{ \AA}$ . We label the diffusion of the vacancy to one of these sites by

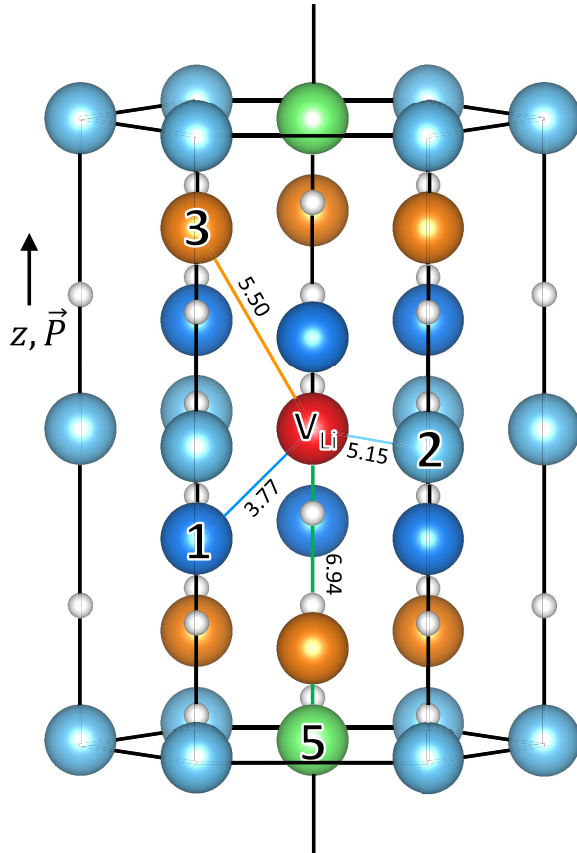


FIG. 7. Nearest-neighbor sites to a  $V_{\text{Li}}$  (represented in red) in  $\text{LiNbO}_3$  and  $\text{LiTaO}_3$ . First-nearest neighbors are in blue, second-nearest neighbors in light blue, and Nb/Ta atoms are white. Oxygen atoms are not shown for the sake of clarity. Distances are given in  $\text{Å}$ .

path A, as represented in Fig. 8. The diffusion of the vacancy will probably not occur along the straight line joining the vacancy and the first neighbor, but will rather run through empty oxygen octahedra, as shown in the right-hand side of the figure. The dashed line is only a guide to the eye; the real diffusion pathway is determined by the NEB method. We remark that the path A has two similar components parallel and perpendicular to the ferroelectric axis. Thus, path A will lead to a nearly isotropic Li diffusion, which is supported by experimental results of Li diffusion on differently oriented single crystals [56].

The considered Li vacancy has furthermore six equivalent second-nearest neighbors (light-blue balls in Fig. 7) at a distance of  $5.15 \text{ Å}$ . A jump of the  $V_{\text{Li}}$  to the second-nearest neighbors is also possible, and qualitatively different from path A. We label this diffusion mechanism as path B. Also, in this case a diffusion through empty oxygen octahedra, as shown in the right-hand side of Fig. 8, is expected to be energetically favored. We remark that the six equivalent second-nearest neighbors all lie on the basal plane, i.e., perpendicular to the ferroelectric axis. Thus, atomic movement along path B leads to an anisotropic Li diffusion.

Further, other neighbors can only be reached through longer diffusion paths that include at least either path A or

path B. Thus, diffusion to further lattice sites is characterized by energy barriers which are at least as high as that of path A or path B, which are therefore the only paths to be considered to determine the migration energy threshold.

The energy barriers associated with the considered paths A and B are shown in Fig. 9. They are of similar magnitude; however, path B is characterized by a somewhat higher energy barrier ( $1.29 \text{ eV}$  for the path A vs  $1.70 \text{ eV}$  for the path B).

The corresponding diffusion paths are shown in Figs. 10 and 11.

As expected, in both cases the diffusion path deviates from the direct line joining start and end configuration, so that the diffusion path is longer than the distance between Li nearest neighbors. The actual diffusion path runs through empty oxygen octahedra. In this way Li ions can maximize the distance between oxygen ions when they cross an oxygen layer. Indeed, the latter is characterized by a high electronic charge density. The minimum-energy path has its energy maxima when the Li atom is between two neighboring Nb atoms, as shown in Fig. 10(b). In the case of path B, a further Li atom is present below the moving ion, which might explain the higher energy barrier.

In a previous work, the Li diffusion in  $\text{LiNbO}_3$  was investigated by a similar computational approach [50]. In that work a diffusion path was found that roughly corresponds to our path A, and is characterized by an energy barrier of  $1.64 \text{ eV}$ . Interestingly, the Li diffusion in the basal plane (path B) was associated with an energy barrier as high as  $5.5 \text{ eV}$ , which is much higher than the value calculated on the present work and which can hardly be explained considering the minimum-energy path.

Repeating the calculations for the Li vacancy diffusion in  $\text{LiTaO}_3$  crystals yields nearly identical results. The minimum-energy path is qualitatively the same as calculated for  $\text{LiNbO}_3$  and shown in Figs. 10 and 11, both in the case of path A and path B. Merely the calculated energy barriers are slightly lower by  $0.06 \text{ eV}$  in the case of path A and by  $0.02 \text{ eV}$  in the case of path B, respectively.

#### IV. DISCUSSION

As a result, we found that for  $\text{LiNbO}_3$  the experimentally determined activation energy of diffusion  $\Delta E = (1.35 \pm 0.02) \text{ eV}$  and the activation energy of electrical conductivity  $E_A = (1.31 \pm 0.04) \text{ eV}$  are in excellent agreement with the migration energy of path A ( $1.29 \text{ eV}$ ). This leads to the conclusion that path A is relevant for the diffusion process together with the experimental result of Li diffusion being identical for differently oriented single crystals [56] (three-dimensional diffusion).

The formation energy of defects does not play a considerable role in the present situation and we get  $\Delta E = \Delta E_m \approx 1.3 \text{ eV}$ . This is justified by the defect model given above in a way that vacancy formation is realized by off stoichiometry (structural vacancies) and not by temperature enhancement (thermally activated vacancies). This means that after crystal growth of congruent crystals as regarded here, vacancies on the Li sublattice of about 4% are present and thermal vacancies are negligible. Over the complete

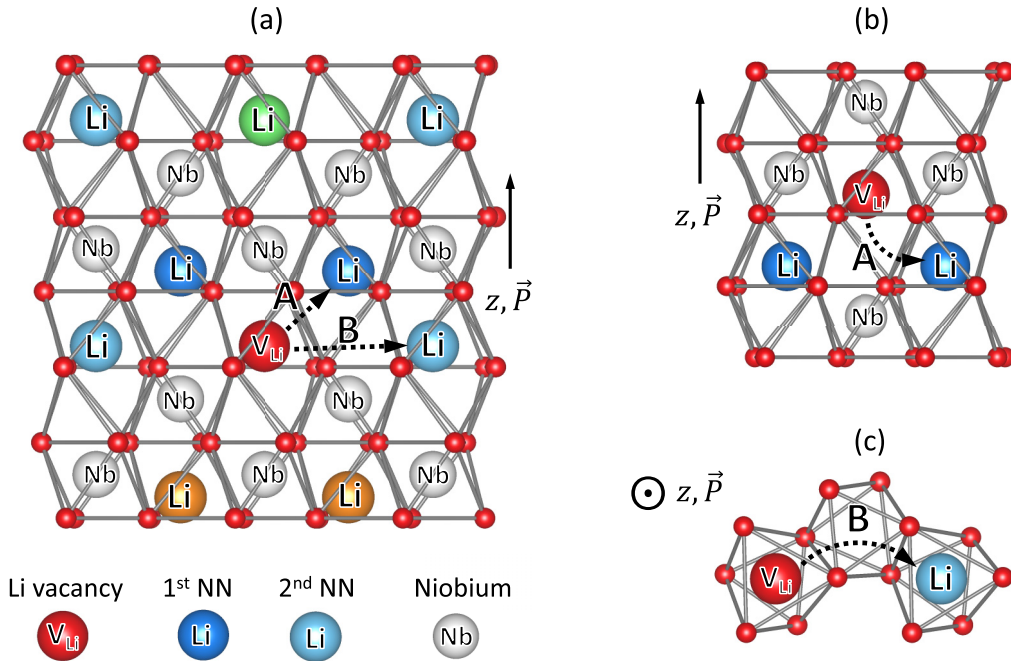


FIG. 8. (a) Diffusion pathways for a  $V_{Li}$  (represented in red). Path A labels a jump to the first-nearest neighbor, while path B labels a jump to the second-nearest neighbor. All other neighbors might be reached by a combination of path A and B. (b), (c) More probable diffusion paths through empty oxygen octahedra are shown. Dashed lines are merely guides to the eye; the real minimum-energy path is determined by NEB method.

investigated temperature range Li vacancies are present and form the dominating defect governing diffusion. For  $LiTaO_3$ , the experimentally determined activation energy of diffusion  $\Delta E = (1.33 \pm 0.04)$  eV and the activation energy of electrical conductivity  $E_A = (1.36 \pm 0.04)$  eV are also very similar to the migration energy calculated for path A (1.23 eV).

For further analysis we assume that the preexponential factor in Eq. (4) is given by

$$D_0 = x a^2 v_0 \exp(\Delta S/k_B), \tag{8}$$

where  $a \approx 3.77$  Å [14] is the Li-Li jump distance,  $x = [V_{Li}]/[Li_{Li}^i] = 0.04$  [52] is the mole fraction of Li

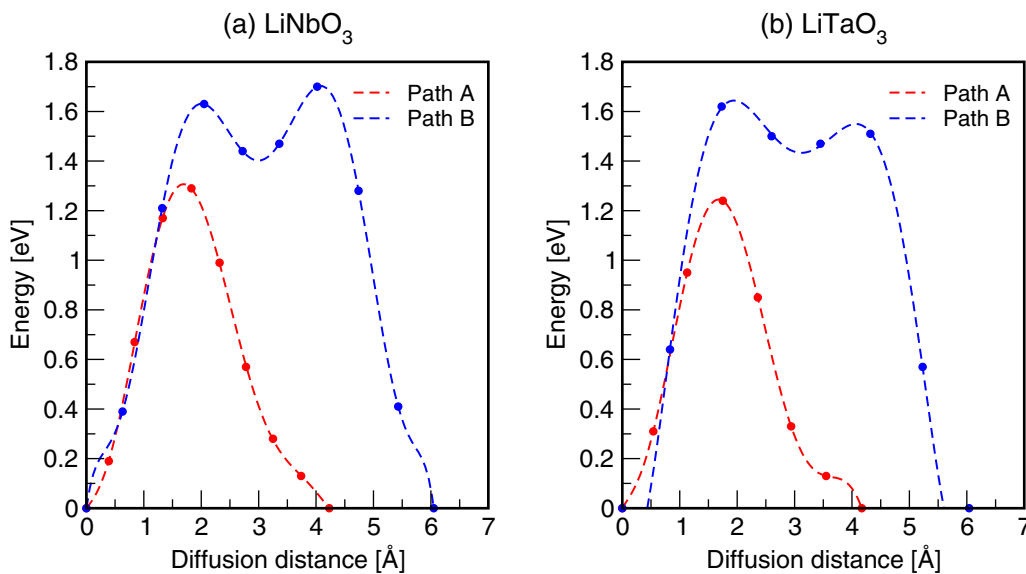


FIG. 9. Energy barriers associated with the  $V_{Li}$  diffusion along path A (red) and along path B (blue) calculated for  $LiNbO_3$  (left-hand side) and  $LiTaO_3$  (right-hand side) with the NEB method and eight or six images, respectively. Dotted lines are polynomial fit of the calculated data.

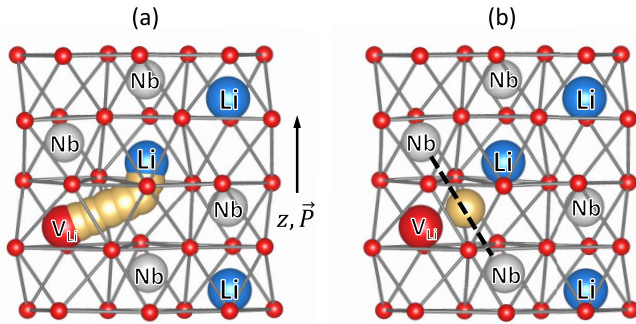


FIG. 10. (a) Calculated minimum-energy path for the lithium vacancy diffusion along path A. (b) The highest energy image is the one at which the Li atom is exactly between two neighboring Nb atoms. Oxygen is red, Li blue, and Nb is white.

vacancies, and  $\nu_0 \approx 2.5 \times 10^{13} \text{ s}^{-1}$  is a characteristic vibration frequency as calculated in Ref. [14]. If the entropy of ionic motion is assumed to be  $\Delta S \approx 0$ , the preexponential factor can be calculated to  $D_0 = 1.4 \times 10^{-7} \text{ m}^2/\text{s}$ . This is in excellent agreement with the experimentally derived value of  $3.1 \times 10^{-7} \text{ m}^2/\text{s}$  within error limits, confirming the suggested model. The product of the geometry factor, including possible hopping sites for Li, and of the correlation factor is approximated to 1 in Eq. (8). This might be different [57,58] but, due to the error attributed to the experimentally derived  $D_0$  value and due to the only estimated quantity  $\Delta S$ , a more detailed analysis is not appropriate here. Note that using the

simple relation  $\nu_0 = kT/h$  in Eq. (8) gives a similar result of  $D_0 = 3.1 \times 10^{-7} \text{ m}^2/\text{s}$  at  $500^\circ\text{C}$ . For  $\text{LiTaO}_3$  the same conclusion can be drawn.

We can also use Eq. (4) together with the experimentally determined data of  $D_0 = 3.1 \times 10^{-7} \text{ m}^2/\text{s}$  and  $\Delta E = 1.35 \text{ eV}$  to calculate the diffusivity at room temperature ( $25^\circ\text{C}$ ) to  $D \approx 10^{-29} \text{ m}^2/\text{s}$ . The computed diffusivity can be employed, in turn, to estimate the diffusion length  $L$  during the time  $t$  as  $L = \sqrt{6Dt}$ . The equation is derived from the random-walk theory assuming isotropic diffusion. This equation shows that at room temperatures timescales of the order of magnitude of years are needed for a lithium ion to diffuse to the first-nearest neighbor site. On the contrary, at  $500^\circ\text{C}$  diffusion of Li ions to the first-nearest neighbor site occurs on the timescale of several microseconds, suggesting a high Li mobility.

### V. CONCLUSION

We carried out investigations on Li tracer self-diffusion in congruent  $\text{LiNbO}_3$  and  $\text{LiTaO}_3$  single crystals up to a temperature of  $800^\circ\text{C}$  using isotope-enriched  $^6\text{LiNbO}_3$  and  $^6\text{LiTaO}_3$  tracer layers, in combination with secondary ion mass spectrometry depth-profile analysis. The results are compared to conductivity measurements done by impedance spectroscopy and to nudged elastic band calculations based on density-functional theory. We found that

- (i) The diffusivities of both isostructural materials are identical within error limits and can be described by the Arrhenius law with an activation energy of about 1.3 eV.
- (ii) This activation energy is in excellent agreement with the energy barrier for the diffusion of a single Li vacancy (next-neighbor jumps) as determined by NEB calculations. This in turn suggests the presence of Li vacancies in high concentrations, thus supporting the  $(\text{Nb}_{\text{Li}}^{\cdot\cdot} + 4\text{V}_{\text{Li}}')$  defect model of congruent composition.
- (iii) The Li-ion conductivities calculated from the diffusivities according to the Nernst-Einstein relation are identical within the error margins with the overall conductivities obtained from impedance spectroscopy measurements. This indicates that Li is the dominating species for the electric conductivity in the temperature range investigated.

Concerning the calculations, it can be assumed that the energy level of elastic bands is mainly influenced by the positions of ions and electrons immediately adjacent to the diffusion path—and not by additional vacancies further away. Therefore, the results can be generalized to the congruent composition to some extent. These assumptions will be tested in further computational studies.

### ACKNOWLEDGMENTS

Financial support from the Deutsche Forschungsgemeinschaft (DFG) in the framework of the research unit FOR5044 (Projects No. SCHM 1569/39-1, No. FR 1301/42-1, No. SA 1948/2-1, No. SU 1261/1-1, and No. GA 2403/7-1) and of the Project No. FR 1301/32-1 is gratefully acknowledged.

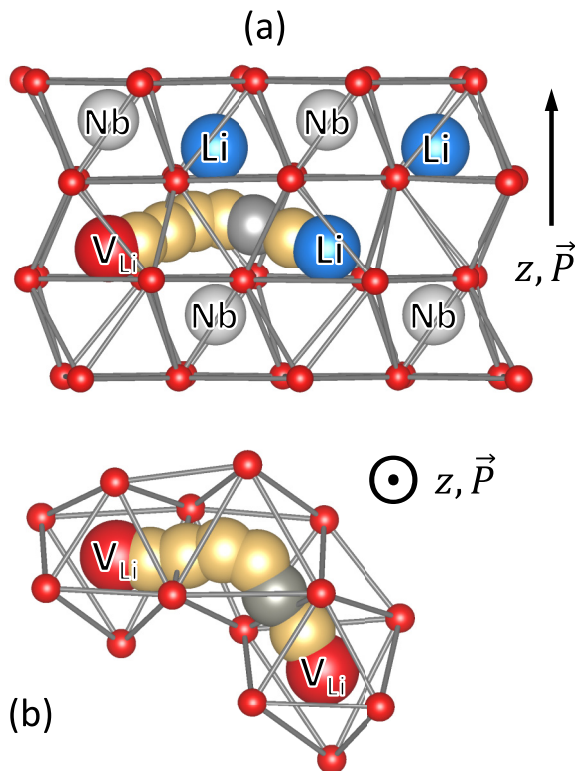


FIG. 11. Calculated minimum energy path for the lithium vacancy diffusion along path B. (a) Side view, (b) top view. The highest energy image is marked in gray. Oxygen is red, Li blue, Nb white.

Calculations for this research were conducted on the Lichtenberg high-performance computer of the TU Darmstadt as well as at the Höchstleistungsrechenzentrum Stuttgart (HLRS). We

further acknowledge computational resources provided by the HPC Core Facility and the HRZ of the Justus-Liebig-Universität Gießen.

- [1] O. Sánchez-Dena, C. D. Fierro-Ruiz, S. D. Villalobos-Mendoza, D. M. Carrillo Flores, J. T. Elizalde-Galindo, and R. Farías, *cryst.* **10**, 973 (2020).
- [2] O. Sánchez-Dena, S. D. Villalobos-Mendoza, R. Farías, and C. D. Fierro-Ruiz, *cryst.* **10**, 990 (2020).
- [3] T. Volk, R. Hull, R. M. Osgood, J. Parisi, H. Warlimont, and M. Wöhlecke, *Lithium Niobate* (Springer, Berlin, 2008).
- [4] *Properties of Lithium Niobate (INSPEC/IEE)*, edited by K.-K. Wong (Institution of Engineering and Technology, London, UK, 2002).
- [5] S. C. Abrahams and P. Marsh, *Acta Crystallogr. B: Struct. Sci.* **42**, 61 (1986).
- [6] S. C. Abrahams, J. M. Reddy, and J. L. Bernstein, *J. Phys. Chem. Solids* **27**, 997 (1966).
- [7] H. D. Megaw, *Acta Crystallogr. A: Cryst. Phys. Diffr. Theor. Gen. Crystallogr.* **24**, 583 (1968).
- [8] R. S. Weis and T. K. Gaylord, *Appl. Phys. A* **37**, 191 (1985).
- [9] P. Lerner, C. Legras, and J. P. Dumas, *J. Cryst. Growth* **3-4**, 231 (1968).
- [10] M. Nakamura, S. Takekawa, S. Kumaragurubaran, and K. Kitamura, *Jpn. J. Appl. Phys.* **47**, 3476 (2008).
- [11] P. F. Bordui, R. G. Norwood, D. H. Jundt, and M. M. Fejer, *J. Appl. Phys.* **71**, 875 (1992).
- [12] Y. Li, W. G. Schmidt, and S. Sanna, *Phys. Rev. B* **91**, 174106 (2015).
- [13] O. F. Schirmer, O. Thiemann, and M. Wöhlecke, *J. Phys. Chem. Solids* **52**, 185 (1991).
- [14] H. Xu, D. Lee, S. B. Sinnott, V. Dierolf, V. Gopalan, and S. R. Phillpot, *J. Phys.: Condens. Matter* **22**, 135002 (2010).
- [15] N. Masaif, S. Jebbari, F. Bennani, and A. Jennane, *Ferroelectr. Lett. Sect.* **32**, 7 (2005).
- [16] A. Vyalikh, M. Zschornak, T. Köhler, M. Nentwich, T. Weigel, J. Hanzig, R. Zaripov, E. Vavilova, S. Gemming, E. Brendler, and D. C. Meyer, *Phys. Rev. Mater.* **2**, 013804 (2018).
- [17] J. Rahn, E. Hüger, L. Dörrer, B. Ruprecht, P. Heitjans, and H. Schmidt, *Phys. Chem. Chem. Phys.* **14**, 2427 (2012).
- [18] *Impedance Spectroscopy*, edited by E. Barsoukov and J. R. Macdonald (Wiley, New York, 2018).
- [19] S. Lanfredi and A. C. M. Rodrigues, *J. Appl. Phys.* **86**, 2215 (1999).
- [20] G. Kresse and J. Furthmüller, *Phys. Rev. B, Condens. Matter* **54**, 11169 (1996).
- [21] G. Kresse and J. Furthmüller, *Comput. Mater. Sci.* **6**, 15 (1996).
- [22] P. E. Blöchl, *Phys. Rev. B, Condens. Matter* **50**, 17953 (1994).
- [23] G. Kresse and D. Joubert, *Phys. Rev. B, Condens. Matter* **59**, 1758 (1999).
- [24] J. P. Perdew, J. A. Chevary, S. H. Vosko, K. A. Jackson, M. R. Pederson, and C. Fiolhais, *Phys. Rev. B, Condens. Matter* **46**, 6671 (1992).
- [25] J. P. Perdew, K. Burke, and M. Ernzerhof, *Phys. Rev. Lett.* **77**, 3865 (1996).
- [26] J. P. Perdew, K. Burke, and M. Ernzerhof, *Phys. Rev. Lett.* **78**, 1396(E) (1997).
- [27] H. J. Monkhorst and J. D. Pack, *Phys. Rev. B* **13**, 5188 (1976).
- [28] H. Jonsson, G. Mills, and K. W. Jacobsen, in *Proceedings of the International School of Physics Computer Simulation of Rare Events and the Dynamics of Classical and Quantum Condensed-Phase Systems; Euroconference on "Technical advances in particle-based computational material sciences," Lerici, 7 July–18 July 1997* (World Scientific, Singapore, 1998), pp. 385–404.
- [29] G. Henkelman and H. Jonsson, *J. Chem. Phys.* **113**, 9978 (2000).
- [30] G. Henkelman, B. P. Uberuaga, and H. Jonsson, *J. Chem. Phys.* **113**, 9901 (2000).
- [31] E. L. Kolsbjerg, M. N. Groves, and B. Hammer, *J. Chem. Phys.* **145**, 94107 (2016).
- [32] D. Sheppard, P. Xiao, W. Chemelewski, D. D. Johnson, and G. Henkelman, *J. Chem. Phys.* **136**, 74103 (2012).
- [33] J. Crank, *The Mathematics of Diffusion* (University Press, Oxford, 2011).
- [34] J. Uhlendorf, B. Ruprecht, E. Witt, C. V. Chandran, L. Dörrer, E. Hüger, F. Strauß, P. Heitjans, and H. Schmidt, *Z. Phys. Chem.* **231**, 1423 (2017).
- [35] E. Hüger, J. Rahn, J. Stahn, T. Geue, P. Heitjans, and H. Schmidt, *Phys. Chem. Chem. Phys.* **16**, 3670 (2014).
- [36] K. Kitamura, Y. Furukawa, K. Niwa, V. Gopalan, and T. E. Mitchell, *Appl. Phys. Lett.* **73**, 3073 (1998).
- [37] A. Krampf, M. Imlau, Y. Suhak, H. Fritze, and S. Sanna, *New J. Phys.* **23**, 33016 (2021).
- [38] A. Huanosta and A. R. West, *J. Appl. Phys.* **61**, 5386 (1987).
- [39] M. N. Palatnikov, V. A. Sandler, A. V. Yatsenko, N. V. Sidorov, S. V. Evdokimov, and O. V. Makarova, *Inorg. Mater.* **51**, 685 (2015).
- [40] D. C. Sinclair and A. R. West, *Phys. Rev. B, Condens. Matter* **39**, 13486 (1989).
- [41] D. Ming, J. M. Reau, J. Ravez, J. Gitae, and P. Hagemuller, *J. Solid State Chem.* **116**, 185 (1995).
- [42] P. Fielitz, O. Schneider, G. Borchardt, A. Weidenfelder, H. Fritze, J. Shi, K. D. Becker, S. Ganschow, and R. Bertram, *Solid State Ionics* **189**, 1 (2011).
- [43] P. Fielitz, G. Borchardt, S. Ganschow, R. Bertram, R. A. Jackson, H. Fritze, and K.-D. Becker, *Solid State Ionics* **259**, 14 (2014).
- [44] P. Dunbar and I. I. I. Birnie, in *Proceedings, Ceramics and Inorganic Crystals for Optics, Electro-Optics, and Nonlinear Conversion* (SPIE, Bellingham, Washington, USA, 1989), pp. 81–87.
- [45] H. H. Nahm and C. H. Park, *Appl. Phys. Lett.* **78**, 3812 (2001).
- [46] P. Giri, A. Biswas, and M. K. Mandal, *J. Inst. Eng. India Ser. D* **102**, 283 (2021).
- [47] T. Köhler, M. Zschornak, C. Röder, J. Hanzig, G. Gärtner, T. Leisegang, E. Mehner, H. Stöcker, and D. C. Meyer, *J. Mater. Chem. C* **11**, 520 (2023).
- [48] B. Ruprecht, J. Rahn, H. Schmidt, and P. Heitjans, *Z. Phys. Chem.* **226**, 431 (2012).

- [49] N. Zotov, H. Boysen, F. Frey, T. Metzger, and E. Born, *J. Phys. Chem. Solids* **55**, 145 (1994).
- [50] H. Xu, D. Lee, J. He, S. B. Sinnott, V. Gopalan, V. Dierolf, and S. R. Phillpot, *Phys. Rev. B* **78**, 174103 (2008).
- [51] J. Rahn, P. Heitjans, and H. Schmidt, *J. Phys. Chem. C* **119**, 15557 (2015).
- [52] J. Shi, H. Fritze, G. Borchardt, and K.-D. Becker, *Phys. Chem. Chem. Phys.* **13**, 6925 (2011).
- [53] W. He, X. Gao, L. Pang, D. Wang, N. Gao, and Z. Wang, *J. Phys.: Condens. Matter* **28**, 315501 (2016).
- [54] Y. Li, S. Sanna, and W. G. Schmidt, *J. Chem. Phys.* **140**, 234113 (2014).
- [55] Y. Li, W. G. Schmidt, and S. Sanna, *Phys. Rev. B* **89**, 094111 (2014).
- [56] J. Rahn, L. Dörrer, B. Ruprecht, P. Heitjans, and H. Schmidt, *Defect Diff. Fusion* **333**, 33 (2013).
- [57] J. Hanzig, M. Zschornak, E. Mehner, F. Hanzig, W. Münchgesang, T. Leisegang, H. Stöcker, and D. C. Meyer, *J. Phys.: Condens. Matter* **28**, 225001 (2016).
- [58] H. Mehrer, *Diffusion in Solids* (Springer, Berlin, 2007).